nature chemical biology

Article

https://doi.org/10.1038/s41589-022-01229-7

A structural basis for prion strain diversity

Received: 21 June 2022

Accepted: 18 November 2022

Published online: 16 January 2023

Check for updates

Szymon W. Manka[1], Adam Wenborn[1], Jemma Betts[1], Susan Joiner[1], Helen R. Saibil[2] ✉, John Collinge[1] ✉ & Jonathan D. F. Wadsworth[1] ✉

Recent cryogenic electron microscopy (cryo-EM) studies of infectious, ex vivo, prion fibrils from hamster 263K and mouse RML prion strains revealed a similar, parallel in-register intermolecular β-sheet (PIRIBS) amyloid architecture. Rungs of the fibrils are composed of individual prion protein (PrP) monomers that fold to create distinct N-terminal and C-terminal lobes. However, disparity in the hamster/mouse PrP sequence precludes understanding of how divergent prion strains emerge from an identical PrP substrate. In this study, we determined the near-atomic resolution cryo-EM structure of infectious, ex vivo mouse prion fibrils from the ME7 prion strain and compared this with the RML fibril structure. This structural comparison of two biologically distinct mouse-adapted prion strains suggests defined folding subdomains of PrP rungs and the way in which they are interrelated, providing a structural definition of intra-species prion strain-specific conformations.

Transmissible spongiform encephalopathies (TSEs) or prion diseases are invariably fatal neurodegenerative disorders affecting mammals and include Creutzfeldt–Jakob disease (CJD) in humans, scrapie in sheep and goats, bovine spongiform encephalopathy (BSE) in cattle and chronic wasting disease (CWD) in cervids[1–3]. Prions, the causative agent of TSEs, are composed of polymeric fibrillar assemblies of misfolded host-encoded cellular prion protein (PrP^C) that propagate by fiber elongation and fission. Biologically distinct prion strains can, however, be serially propagated in identical hosts expressing the same PrP^C and produce different disease phenotypes. Understanding the structural basis of prion strain diversity is, therefore, of considerable biological interest and evolutionary significance. In addition, prions may transmit disease between mammalian species, as with the infection of humans with BSE prions causing variant CJD. Such cross-species transmission is limited by so-called species barrier effects that relate to structural compatibility of prion strains with host PrP^C according to the conformational selection model[2,4]. As it is well recognized that novel prion strains with altered host ranges can arise as a result of PrP polymorphisms in both inter-species and intra-species transmissions[2–6], determining the structural basis of prion diversity is critical to understanding whether emerging animal prion strains constitute a zoonotic risk to public health[2–7].

The prion concept has, however, extended well beyond propagation of assemblies of PrP with the discovery of yeast prions[8]. A number of proteins in yeast and other fungi can form prions and demonstrate strain diversity related to well-characterized structural differences[9]; prions of fungi are also not always deleterious to a host[9]. Additionally, all the common neurodegenerative diseases are associated with accumulation of assemblies of host-encoded peptides or proteins, and inoculation studies in suitable transgenic mice have demonstrated the ability of such pathology to be seeded and anatomically spread in a new host, suggesting the involvement of prion-like mechanisms in their pathogenesis[3,10–13]. The relevance of such experimental transmission of the amyloid-β pathology seen in Alzheimer's disease (AD) to human disease is now clear with the recognition and experimental confirmation of iatrogenic seeding of parenchymal and vascular amyloid-β pathology between humans via cadaver-derived human pituitary extracts[3,14,15]. Indeed, it is now clear that cerebral amyloid angiopathy (CAA) is a prion disease[15]. Assuming, after even longer incubation periods, that such recipients of amyloid-β and tau-contaminated cadaver-derived material also develop a tauopathy in addition to the widespread amyloid-β pathology, thereby meeting the full neuropathological criteria for AD, this would indicate that AD can also result from such iatrogenic exposure to proteopathic seeds and could be considered a prion disease[3,15]. Conformational selection and the general model of prion strains[2,4] strongly suggests that the prion strain phenomenon will also contribute to the marked phenotypic diversity seen in the commoner neurodegenerative diseases. Indeed, evidence for structural variation in amyloid-β fibrils from distinct clinical subtypes of AD has been reported[12], and remarkable recent progress with structural characterization of diverse

[1]MRC Prion Unit at UCL, Institute of Prion Diseases, University College London, London, UK. [2]Department of Biological Sciences, Institute of Structural and Molecular Biology, Birkbeck College, University of London, London, UK. ✉e-mail: h.saibil@bbk.ac.uk; jc@prion.ucl.ac.uk; j.wadsworth@prion.ucl.ac.uk

https://doi.org/10.1038/s41589-022-01229-7

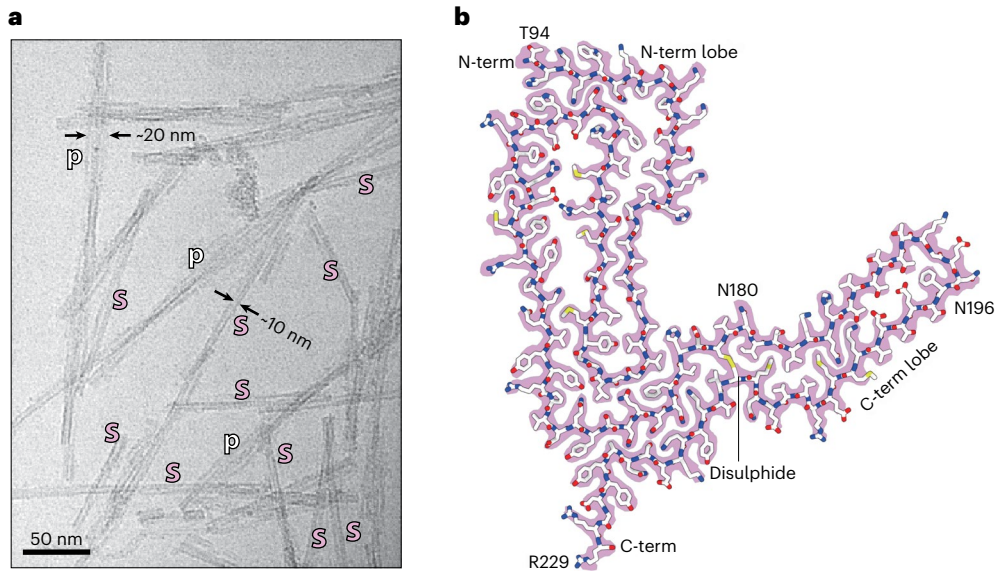

Fig. 1 | ME7 fibril morphologies and the atomic structure of their constituent PrP subunit. a, Representative cryo-EM image from a dataset comprising 6,370 multi-frame movies (300-kV FEI Krios G3i, K3 camera) showing examples of single ME7 protofilaments (s) alongside their paired assemblies (p) with their approximate diameters. **b**, Protein-only density of a single amyloid rung (pink) with the fitted atomic model of the mouse PrP chain shown with sticks colored by heteroatom: C, white; N, blue; O, red; S, yellow. The start (T94) and end (R229) residues of the fitted polypeptide and both N-glycosylation sites are indicated.

self-propagating assemblies of tau, amyloid-β, α-synuclein and TDP-43 from human brain is now facilitating the detailed exploration of the role for strains in determining phenotype[16–19].

Although it is now firmly established that mammalian prions causing TSEs are composed of fibrillar assemblies of misfolded host-encoded PrP (classically designated as PrP^{Sc} (ref. 1)) and propagate by means of seeded protein polymerization and fission[1–3,20–24], the structural mechanisms underpinning prion strain diversity remain unclear. Although it is known that prion strains represent distinct misfolded PrP conformations and assembly states[1–3,25–29], high-resolution structural definition of prion strains has been extremely problematic. In this regard, because in vitro synthetically generated PrP amyloids are either devoid of detectable prion infectivity or have specific infectivities too low for meaningful structural analysis[2,3,21,30], efforts to define authentic infectious prion structures have to overcome the difficulty of isolating relatively homogeneous ex vivo prion strain assemblies of correspondingly extremely high specific infectivity suitable for structural analysis[21,31]. Recently, however, significant progress has been made[22–24].

High-resolution cryogenic electron microscopy (cryo-EM) studies of infectious, ex vivo prions isolated from the hamster 263K prion strain[22] or the mouse RML prion strain[23] reported single protofilament helical amyloid fibrils that have a broadly similar, parallel in-register intermolecular β-sheet (PIRIBS) amyloid architecture. Rungs of the fibrils are composed of single PrP monomers that fold to create distinct N-terminal and C-terminal lobes with the N-linked glycans and glycosylphosphatidylinositol (GPI) anchor projecting from the C-terminal lobe[22,23]. Transgenic mice expressing GPI anchorless PrP when infected with RML prions generated in wild-type mice propagate aRML prion fibrils that have the same fold as seen in RML prion-infected wild-type mice[23,24]. The overall architectures of hamster 263K and mouse RML fibrils are remarkably similar and compatible with the defining physicochemical properties of prions[22–24].

Despite the overall similarity of the hamster 263K and mouse RML prion fibril architectures, there are pronounced differences in the fold of the C-terminal lobes[23,24], which may be attributable to differences in PrP amino acid sequence and/or distinct conformations associated with divergent prion strains. To determine directly which conformational differences can be attributed to prion strain, comparison of structures of different strains propagated in the same host with identical PrP^{C} substrate is necessary.

Here we report a 2.6-Å cryo-EM structure of fibrils present in highly infectious prion rod preparations isolated from the brain of mice infected with the ME7 mouse-adapted scrapie prion strain[31,32]. Like RML prions[23], ME7 prion rods are predominantly single protofilament helical amyloid fibrils that coexist with paired protofilaments. Crucially, the fibrils of both mouse prion strains share the same underlying modular architecture but with markedly altered topology. We identified conformationally conserved and variable regions in the N-terminal lobe and a structurally congruent, but differently oriented, disulphide-stapled (DS) hairpin in the C-terminal lobe. ME7 and RML strain diversity appears to be linked to the divergent fold of the conformationally variable region and the orientations of the N-terminal and C-terminal lobes, resulting in distinct helical assemblies.

Results

ME7 fibril morphologies resemble those of RML

ME7 prion rods were purified to ~99% purity with respect to total protein from the brain of terminally infected C57Bl/6 mice (Extended Data Fig. 1). We employed the same established method[31] as for the analogous RML preparations[23], which includes proteinase K (PK) treatment of crude brain homogenate and the addition of phosphotungstate (PTA) polyanions that were shown to decorate RML prion fibrils[23] without affecting the protofilament structure[23,24]. Mass spectrometry analyses (provided in a Source Data file) showed that PK N-terminally truncates PrP monomers in ME7 rods at the same site as in RML rods[23], leaving PrP subunits predominantly starting at residue 89 and extending to the C-terminus with intact GPI anchor. Prion infectivity of purified ME7 prions was measured using the Scrapie Cell End Point Assay[31,33–35] (Supplementary Table 1) with titers consistent with previous findings[31,36,37]. As before[23,37], prion rods were the only visible polymers in micrographs with the exception of occasional collagen fibers, amorphous aggregates or vesicles.

Among predominantly single protofilament fibrils (~10-nm apparent diameter), distinctive paired assemblies with the apparent diameter of ~20 nm were also observed in approximately 15% of the micrographs (Fig. 1a). As with the previously reported RML pairs, it remains unclear

https://doi.org/10.1038/s41589-022-01229-7

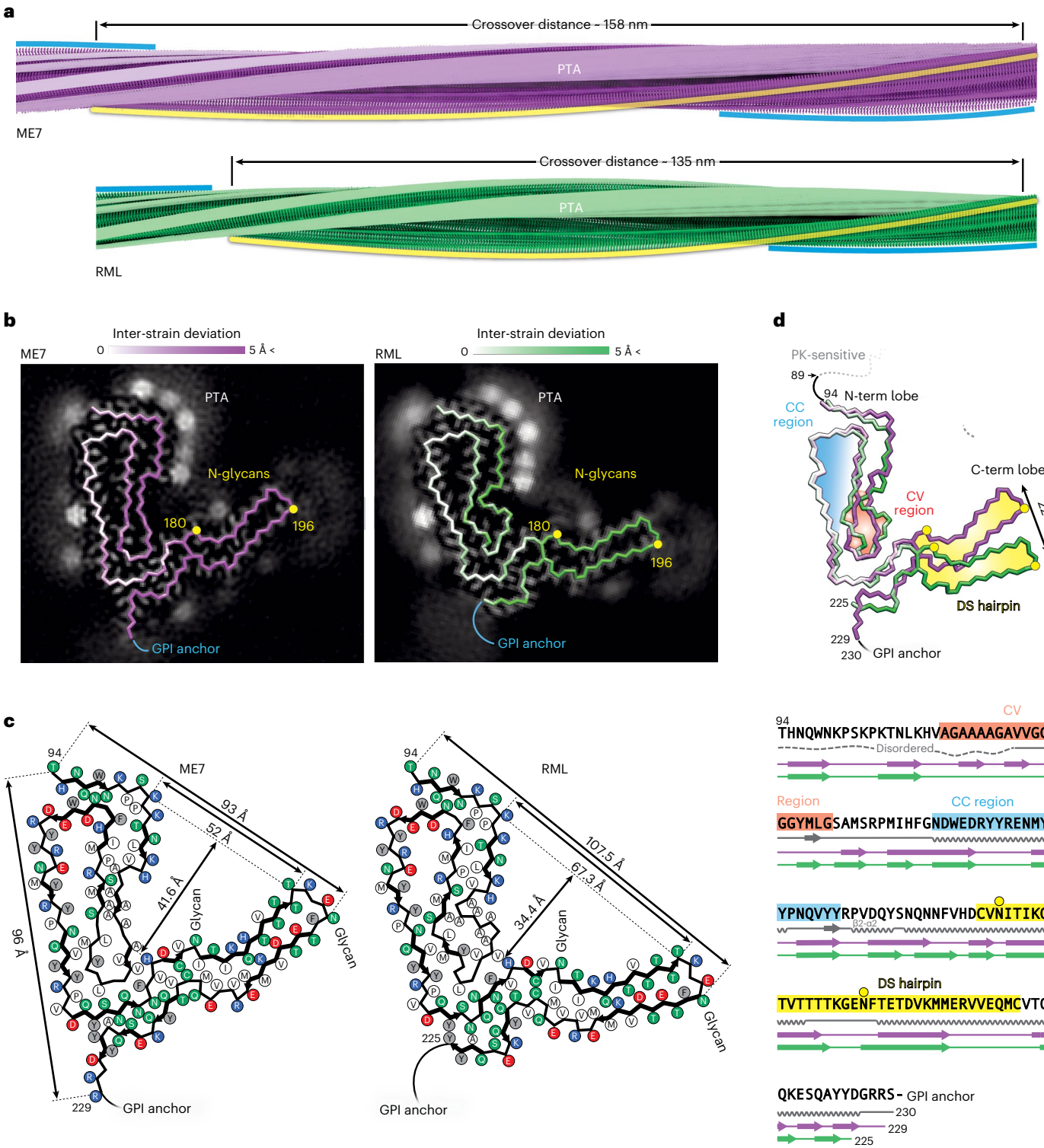

Fig. 2 | Comparison of ME7 and RML protofibrils and assignment of folding subdomains in their core. a, Rendered density views of the helix crossover or half-pitch (180° helical turn) distance, with annotated locations of PTA polyanions (semi-transparent white), N196 (yellow) and GPI anchor (blue). **b**, Density cross-sections with overlaid PrP backbone models colored by relative deviation based on global 3D alignment (UCSF Chimera; **d**), with annotations corresponding to **a**. C-α atoms of both N-glycosylation sites (N180 and N196) are marked with yellow circles. **c**, Diagrams of the PrP subunits with approximate dimensions of the inter-lobe grooves and the longest C-α distances in each model, measured between the indicated C-α atoms (dotted lines). Positions of amino acid side chains are shown with circles (positively charged, blue; negatively charged, red; neutral, green; hydrophobic, white; aromatic, gray) on either side of the backbone (black line). β-strands are indicated with thick black arrowheaded lines. **d**, Top, superposition of PrP backbones colored as in **b** and shaded according to the folding subdomain assignment. N-glycosylation sites are marked with yellow circles. PK-resistant core starts with residue 89. Bottom, mouse PrP sequence from the start of the amyloid core (T94) to the C-terminus (S230-GPI anchor), with color-coded folding subdomain assignment. Secondary structure annotation for PrP^C (gray), ME7 fibril (magenta) and RML fibril (green) is included below the sequence (α-helix, zig-zag; β-sheet, arrow; disordered, undulated dashed line). Start and end residues are numbered, and the β2-α2 region of PrP^C is indicated. N-glycosylation sites (N180 and N196) are marked with yellow circles.

https://doi.org/10.1038/s41589-022-01229-7

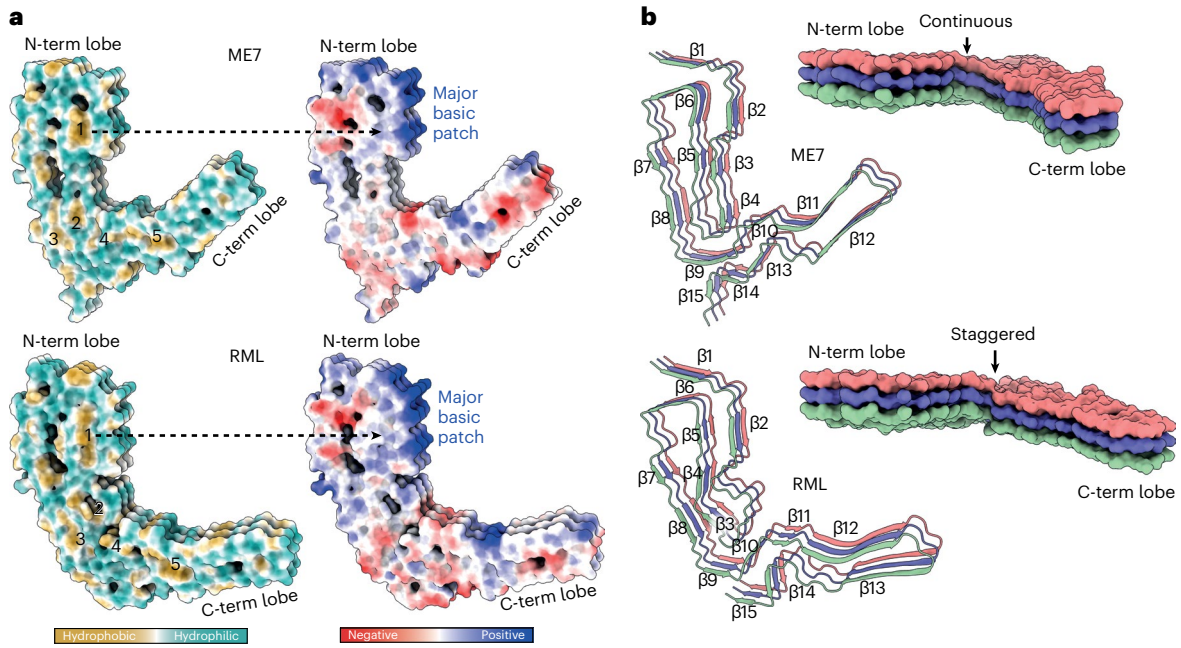

Fig. 3 | Hydrophobic and polar domains of mouse prion protofibrils and details of their PIRIBS arrangements. Models of three consecutive PrP rungs shown as: **a**, solvent-excluded surface colored by hydrophobicity and by electrostatic charge distribution (ChimeraX), and hydrophobic clusters are labeled 1–5; **b**, ribbons with secondary structures and solvent-excluded surface models colored by chain.

if or how PTA may influence the protofilament pairing[23]. Thus, here we focus on single ME7 protofilaments and on how they relate to the previously reported RML protofilaments[23], whose structure is demonstrably not perturbed by PTA[24].

We determined a 2.6-Å-resolution structure of the single ME7 protofilament and found that the fold of its constituent PrP subunit closely resembles that of the RML protofilament, including the double-hairpin N-terminal lobe and a single-hairpin DS C-terminal lobe, with four additional C-terminal residues stabilized as part of the amyloid core in the ME7 fibril (94–229) compared to the RML fibril (94–225) (Fig. 1b, Supplementary Table 2 and Supplementary Figs. 1 and 2). We, thus, appended the remaining D226–R229 residues to the previously built model[23] and then fitted and refined that C-terminally extended model in the cryo-EM density of ME7 (Fig. 1b and Supplementary Table 2).

General comparison of ME7 and RML protofibrils

Akin to the previously reported RML protofilaments[23,24], the ME7 protofilaments comprise a helical PIRIBS ribbon, where each two-lobed rib or rung is formed by a single PrP chain (Fig. 2a,b and Extended Data Fig. 2a,b). The left-handed twist of the ME7 fibril is slightly slower than that of the RML fibril (approximately −0.54° versus −0.64° per rung, respectively), which results in a longer crossover distance (approximately 1,585 Å versus 1,344 Å, respectively) (Fig. 2a). Spacing between the ME7 rungs was estimated at approximately 4.79 Å, whereas, in RML, it was at approximately 4.82 Å (ref. 23), but, given the uncertainty of the pixel size calibration for each magnification (different in each dataset), these spacings can likely be considered essentially the same (~4.8 Å).

The extra (non-protein) densities surrounding the N-terminal lobe of the ME7 reconstruction are consistent with PTA cages ($[PW_{11}O_{39}]^{7-}$ at pH 7.8), previously seen in corresponding locations (basic residues) around RML rods purified with the same method[23] (Fig. 2a–c and Extended Data Fig. 2a,b). The fainter extra densities around the C-terminal lobe of the ME7 reconstruction are also consistent with those previously seen around RML protofilaments[23] and correspond to N180-linked and N196-linked glycans of variable occupancy and the flexible GPI anchor at the C-terminus (Fig. 2b and Extended Data Fig. 2a). There are also likely at least two additional weak PTA-binding sites at residues K184 and K220 in the C-terminal lobe of ME7 and one at residue K184 in the C-terminal lobe of RML; both strains also show weak areas of unassigned density around the hydrophobic patch V202–M204 (compare Fig. 2b,c).

In each strain, the N180 glycan stems from the base of the C-terminal lobe and occupies the groove between the two lobes, which is significantly narrower and deeper in the ME7 fibril than that in the RML fibril (approximately 52 × 41.6 Å versus 67.3 × 34.4 Å, respectively) (Fig. 2b–d and Extended Data Fig. 2a,b). The N196 glycan and GPI anchor project outward in a roughly similar fashion in each fibril (Fig. 2a–c). Considering the protein backbone, the widest dimension of the ME7 rung is shorter than that of RML (96 Å versus 107.5 Å, respectively) and falls between the first (T94) and the last (R229) residue of the amyloid core (one residue away from the GPI anchor), whereas that of RML falls between the first residue of the amyloid core (also T94) and N196 (the second glycosylation site) (Fig. 2c).

Common PrP folding subdomains in ME7 and RML protofibrils

Global three-dimensional (3D) alignment of the PrP monomer from the ME7 fibril with that from the RML fibril reveals regions of conserved and of variable conformation (Fig. 2b,d). The N-terminal lobe can be subdivided into two folding subdomains on that basis. The tip of the first hairpin contains the Ala/Gly-rich sequence (A112–G130), which adopts a modestly different conformation in the two strains (Fig. 2b–d and Extended Data Fig. 2c) and is hereafter designated the conformationally variable (CV) region. Crucially, this CV region interfaces with the C-terminal lobe, and, thus, its conformation may impact the spatial arrangement of the two lobes (Fig. 2d). Conversely, the tip and the external half of the second hairpin (N142–Y162) have closely superimposable conformations in both strains (<1-Å root mean square deviation (RMSD)) (Fig. 2b,d and Extended Data Fig. 2c); we, therefore, designate this the conformationally conserved (CC) region. The DS hairpin of the C-terminal lobe, which harbors the two glycosylation sites, is also nearly superimposable between the two strains (<1-Å RMSD), although it is

https://doi.org/10.1038/s41589-022-01229-7

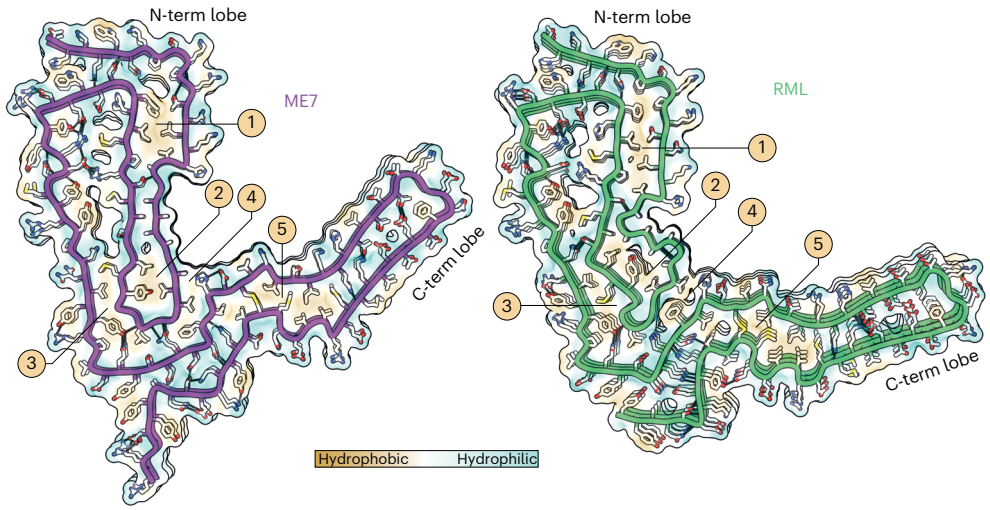

Fig. 4 | Lateral interactions stabilizing mouse prion fibrils. Depiction of polar and non-polar lateral contacts. Protein backbone is shown with cartoon (licorice) representation, amino acid side chains as white sticks colored by heteroatom (O, red; N, blue; S, yellow) and selected hydrogen bonds as black lines. The hydrophobic patches are numbered 1–5.

markedly displaced (by 22 Å at the tip) in the ME7 structure compared to the RML structure, in line with the altered configuration of the CV region (Fig. 2d and Extended Data Fig. 2c).

Other common structural regions in ME7 and RML protofibrils

K100–H110 region forms a major basic patch in the N-terminal lobe of both fibrils and faces the N180 glycan in the groove of the fibril (Figs. 2b,c and 3a,b). This basic patch appears to be firmly stabilized by the first of the five major intra-chain hydrophobic clusters (mainly P101, P104, L108, V111, P136, I138 and F140), in both ME7 and RML fibrils (Figs. 2b,3a and 4). The second and third major hydrophobic clusters (mainly V121, Y126, L128 and L123, M127, V160, Y162 and P164, respectively) appear to stabilize variable configurations of the CV region within the N-terminal lobe, whereas the fourth major hydrophobic cluster provides the third hydrophobic anchor point for the CV region at the inter-lobe interface in both protofibrils (Figs. 2c,3a and 4). This hydrophobic interface involves the N-terminal lobe's residue V120 and the C-terminal lobe's residues F174 and H176 in both RML and ME7 folds and, additionally, N-terminal lobe's residue A119 in the ME7 fold only (Figs. 2c and 4). Finally, the fifth major hydrophobic cluster (I181, I183, M205, V208, V209 and M212) precedes and encompasses the base of the DS hairpin (spanning both sides of the disulphide bond), likely conferring rigidity to the DS hairpin fold in both structures (Figs. 2c,3a and 4). Of note, the interaction of V175 with V214 in the ME7 protofibril is replaced by a less favorable interaction with T215 in RML (Fig. 2c).

Distinct PIRIBS arrangement in ME7 and RML protofibrils

There are 15 inter-chain β-sheets (or PIRIB-sheets) in ME7 and RML protofibril structures, but their arrangement is not identical (Figs. 2c,d and 3b). The largest variation in the β-sheet distribution is seen in the CV region, and the highest conservation of that is seen in the CC region (β-strands 6–8) and the DS hairpin (β-strands 10–12 in ME7 and 11–13 in RML) (Figs. 2c,d and 3b). Intervening regions also show variations in the PIRIBS arrangement (Figs. 2c,d and 3b), but the first two β-strands that accompany the major basic patch are conserved (Figs. 2c,3a,b and 4). The PIRIBS architecture defines the main longitudinal polar inter-chain interactions, the inter-rung hydrogen bonds, but, besides the hydrophobic interactions described earlier, there are also lateral intra-chain and inter-chain hydrogen bonds that stabilize both folds (Fig. 4).

Notably, all types of lateral associations between neighboring strands are not exactly co-planar but staggered by ~half-rung distance along the helical axis (that is, running between rungs). The most pronounced stagger (by nearly one rung) is seen at the inter-lobe interface of the RML protofibril (that is, the N-terminal lobe of the rung *i* interacts with the C-terminal lobe of mainly the rung *i* + 1). In the ME7 protofibril, this interface is more continuous, showing the standard ~half-rung stagger (that is, the N-terminal lobe of the rung *i* interacts equally with C-terminal lobes of the rungs *i* and *i* + 1) (Fig. 3b).

Discussion

The infectious RML and ME7 mouse prion protofibril structures compared here show a remarkably similar modular architecture, comprising two conformationally congruent modules (the CC region in the N-terminal lobe and the DS hairpin in the C-terminal lobe) connected by a CV module (the CV region) at the core of the assembly (Fig. 5). A similar overall architecture is seen in the hamster 263K protofibril[22–24] (Extended Data Fig. 3). Comparison of the three folds suggests that the low-complexity (Gly/Ala-rich) region of PrP (residues 112–130) (Fig. 5b) that comprises the CV region is likely amenable to a greater range of misfolded configurations, whereas other more complex regions of sequence that comprise the CC region and DS hairpin (Fig. 5b) may be more conformationally restricted (Extended Data Fig. 3). Of note, in all three folds, the inter-lobe interface involves interaction of residues of the CV region with residues that comprise the β2-α2 loop in the normal PrP^{C} fold (residues 165–175)[38–40] (Fig. 2d and Extended Data Fig. 3). Variation of amino acid sequence within the β2-α2 loop has substantial effects on numerous interspecies prion transmission barriers[41–45], and the CV region contains the 127 G/V and 129 M/V polymorphisms of human PrP that profoundly affect prion disease susceptibility, phenotype and strain selection[2–4,29,46]. Thus the inter-lobe interface appears to be a critical structural determinant of conformational selection linking strains and prion transmission barriers. Although structures of protofibrils from other prion strain/host combinations are clearly required to inform on the generalizability of these new findings, these data now suggest an initial structural framework underpinning prion strain diversity in mammals. In this regard, the new cryo-EM structures coupled with the general similarity of PrP 27–30 truncated PrP^{Sc} banding patterns seen across multiple human and animal prion strains firmly point to a commonality of PIRIBS-based fibrillar architectures.

Notably, the K100–H110 sequence is part of the disordered N-terminal domain in PrP^{C} (refs. 38–40) (Fig. 2d), but, in both mouse (ME7 and RML) protofibrils and in the hamster 263K protofibril, that

https://doi.org/10.1038/s41589-022-01229-7

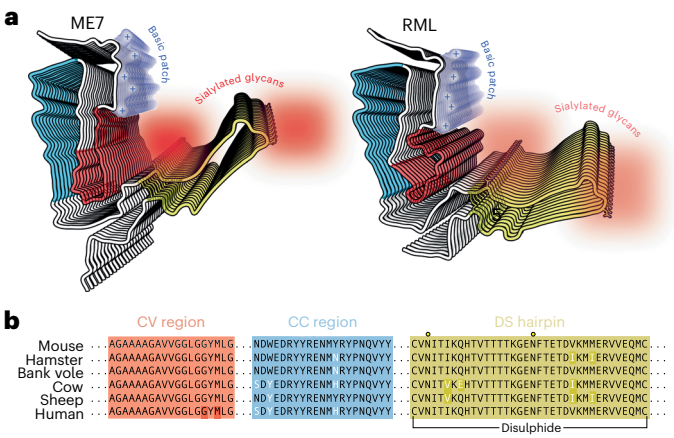

Fig. 5 | Summary of structural differences between ME7 and RML prion protofibril structures. a, Licorice backbone models (ChimeraX) of ME7 and RML protofibrils colored according to PrP^{Sc} folding subdomains (blue, CC region; red, CV region; yellow, DS hairpin; white, intervening regions). Positive charge of the major basic patch (transparent surface) is indicated with + signs, and the sialoglycan occupancy corresponds to the intensity of red shading. The N-glycosylation sites (N180 and N196 side chains) and the disulphide bond are shown as sticks and colored by heteroatom (C, yellow; N, blue; O, red; S, yellow). **b**, Alignment of PrP sequences from different mammals focused on the PrP^{Sc} folding subdomains. Human residues 127 and 129 in the CV region (highlighted with dark red) are polymorphic (G/V and M/V, respectively).

amino acid stretch forms a common physicochemical motif, the major basic patch, around the second β-strand of the N-terminal lobe (compare Figs. 2c,3a,b and 5a and Extended Data Fig. 3)[22–24]. This basic patch faces the N180 glycan in both RML and ME7 mouse protofibrils and also in the hamster protofibril[22–24] and may, therefore, interact with sialylated N180 glycans. However, PTA polyanions used in our ex vivo prion fibril preparations clearly line the major basic patch of both mouse prion protofibrils (Fig. 2b) and, in turn, change its charge from positive to negative. This change does not unify the geometry of ME7 and RML protofibrils, suggesting that the strain-specific topology of the N-terminal and C-terminal lobes in mature prion strains is locked by the PIRIBS architecture alone and that the folds do not depend on long-range sialylated glycan–protein interactions. This deduction is firmly supported by the finding that the wild-type RML fibril fold can be stably propagated using mouse PrP lacking post-translational modifications[23,24] and the demonstration that RML and ME7 prion fibrils purified with PTA faithfully retain their strain-specific transmission properties in mice[31]. The fact that PTA decoration of RML and ME7 fibrils appears to have no significant impact on strain-specific biological activity directly attests to the biological relevance of the fibril folds that we report. Notably, although maintenance of the strain-specific RML and ME7 fibril folds does not appear to rely upon long-range sialylated glycan–protein interactions, the incorporation of particular PrP glycoforms into nascent prion fibrils at the inception of the strain may critically determine the configuration of the fold[23].

The protease-resistant cores and PrP glycoform ratios of purified RML, ME7 and 263K prion fibrils are congruent with the PrP 27–30 truncated PrP^{Sc} banding patterns seen on western blots of PK-digested crude brain homogenates[22,23,31]. All three strains have distinct PrP glycoform ratios, with both the 263K and ME7 strains having a greater proportion of di-glycosylated PrP than the RML strain, which contains relatively more mono-glycosylated and non-glycosylated PrP chains. As stacking of solely di-glycosylated PrP chains into a PIRIBS architecture does not appear energetically prohibitive[47], and comparison of the cross-sections of the RML, ME7 and 263K single protofilaments (Extended Data Fig. 3) does not suggest an obvious steric basis for glycoform selection, it remains unclear how the single protofibril architectures might dictate glycoform composition. On this basis, and as previously proposed[23], we suggest that paired fibril assemblies may have a critical role in determining prion strain-specific PrP glycoform signatures. These pairs currently represent a minor subpopulation (10–15%) of assemblies observed in our RML and ME7 fibril preparations. However, we do not know how different prion purification methods may distort the true (in vivo) content of the pairs. For example, PTA cages are found adjacent to various pairing interfaces and may be disruptive[23]. Whether relatively harsh purification conditions used by others—for example, 1.7 M NaCl (ref. 22)—may also be disruptive remains to be established. Structural investigation of the pairs purified without PTA is currently ongoing and may shed more light on how prion strain-specific glycoform ratios are generated.

Online content

Any methods, additional references, Nature Portfolio reporting summaries, source data, extended data, supplementary information, acknowledgements, peer review information; details of author contributions and competing interests; and statements of data and code availability are available at https://doi.org/10.1038/s41589-022-01229-7.

References

1. Prusiner, S. B. Prions. *Proc. Natl Acad. Sci. USA* **95**, 13363–13383 (1998).
2. Collinge, J. & Clarke, A. A general model of prion strains and their pathogenicity. *Science* **318**, 930–936 (2007).
3. Collinge, J. Mammalian prions and their wider relevance in neurodegenerative diseases. *Nature* **539**, 217–226 (2016).
4. Collinge, J. Variant Creutzfeldt–Jakob disease. *Lancet* **354**, 317–323 (1999).
5. Wadsworth, J. D., Asante, E. A. & Collinge, J. Contribution of transgenic models to understanding human prion disease. *Neuropathol. Appl. Neurobiol.* **36**, 576–597 (2010).
6. Moreno, J. A. & Telling, G. C. Insights into mechanisms of transmission and pathogenesis from transgenic mouse models of prion diseases. *Methods Mol. Biol.* **1658**, 219–252 (2017).
7. Watson, N. et al. The importance of ongoing international surveillance for Creutzfeldt–Jakob disease. *Nat. Rev. Neurol.* **17**, 362–379 (2021).
8. Wickner, R. B. [URE3] as an altered *URE2* protein: evidence for a prion analog in *Saccharomyces cerevisiae*. *Science* **264**, 566–569 (1994).
9. Wickner, R. B., Edskes, H. K., Son, M., Wu, S. & Niznikiewicz, M. Innate immunity to prions: anti-prion systems turn a tsunami of prions into a slow drip. *Curr. Genet.* **67**, 833–847 (2021).
10. Jucker, M. & Walker, L. C. Self-propagation of pathogenic protein aggregates in neurodegenerative diseases. *Nature* **501**, 45–51 (2013).
11. Goedert, M. Alzheimer's and Parkinson's diseases: the prion concept in relation to assembled Aβ, tau, and α-synuclein. *Science* **349**, 1255555 (2015).
12. Qiang, W., Yau, W. M., Lu, J. X., Collinge, J. & Tycko, R. Structural variation in amyloid-β fibrils from Alzheimer's disease clinical subtypes. *Nature* **541**, 217–221 (2017).
13. Carlson, G. A. & Prusiner, S. B. How an infection of sheep revealed prion mechanisms in Alzheimer's disease and other neurodegenerative disorders. *Int. J. Mol. Sci.* **22**, 4861 (2021).
14. Jaunmuktane, Z. et al. Evidence for human transmission of amyloid-β pathology and cerebral amyloid angiopathy. *Nature* **525**, 247–250 (2015).
15. Purro, S. A. et al. Transmission of amyloid-β protein pathology from cadaveric pituitary growth hormone. *Nature* **564**, 415–419 (2018).
16. Shi, Y. et al. Structure-based classification of tauopathies. *Nature* **598**, 359–363 (2021).

17. Sawaya, M. R., Hughes, M. P., Rodriguez, J. A., Riek, R. & Eisenberg, D. S. The expanding amyloid family: structure, stability, function, and pathogenesis. *Cell* **184**, 4857–4873 (2021).
18. Kovacs, G. G., Ghetti, B. & Goedert, M. Classification of diseases with accumulation of tau protein. *Neuropathol. Appl. Neurobiol.* **48**, e12792 (2022).
19. Tarutani, A. et al. Ultrastructural and biochemical classification of pathogenic tau, α-synuclein and TDP-43. *Acta Neuropathol.* **143**, 613–640 (2022).
20. Caughey, B. & Kraus, A. Transmissibility versus pathogenicity of self-propagating protein aggregates. *Viruses* **11**, 1044 (2019).
21. Terry, C. & Wadsworth, J. D. F. Recent advances in understanding mammalian prion structure: a mini review. *Front. Mol. Neurosci.* **12**, 169 (2019).
22. Kraus, A. et al. High-resolution structure and strain comparison of infectious mammalian prions. *Mol. Cell* **81**, 4540–4551 (2021).
23. Manka, S. W. et al. 2.7Å cryo-EM structure of ex vivo RML prion fibrils. *Nat. Commun.* **13**, 4004 (2022).
24. Hoyt, F. et al. Cryo-EM structure of anchorless RML prion reveals variations in shared motifs between distinct strains. *Nat. Commun.* **13**, 4005 (2022).
25. Bessen, R. A. & Marsh, R. F. Distinct PrP properties suggest the molecular basis of strain variation in transmissible mink encephalopathy. *J. Virol.* **68**, 7859–7868 (1994).
26. Telling, G. C. et al. Evidence for the conformation of the pathologic isoform of the prion protein enciphering and propagating prion diversity. *Science* **274**, 2079–2082 (1996).
27. Collinge, J., Sidle, K. C., Meads, J., Ironside, J. & Hill, A. F. Molecular analysis of prion strain variation and the aetiology of 'new variant' CJD. *Nature* **383**, 685–690 (1996).
28. Safar, J. et al. Eight prion strains have PrP^{Sc} molecules with different conformations. *Nat. Med.* **4**, 1157–1165 (1998).
29. Wadsworth, J. D. et al. Human prion protein with valine 129 prevents expression of variant CJD phenotype. *Science* **306**, 1793–1796 (2004).
30. Schmidt, C. et al. A systematic investigation of production of synthetic prions from recombinant prion protein. *Open Biol.* **5**, 150165 (2015).
31. Wenborn, A. et al. A novel and rapid method for obtaining high titre intact prion strains from mammalian brain. *Sci. Rep.* **5**, 10062 (2015).
32. Zlotnik, I. & Rennie, J. C. Further observations on the experimental transmission of scrapie from sheep and goats to laboratory mice. *J. Comp. Path.* **73**, 150–162 (1963).
33. Klohn, P., Stoltze, L., Flechsig, E., Enari, M. & Weissmann, C. A quantitative, highly sensitive cell-based infectivity assay for mouse scrapie prions. *Proc. Natl Acad. Sci. USA* **100**, 11666–11671 (2003).
34. Mahal, S. P. et al. Prion strain discrimination in cell culture: the cell panel assay. *Proc. Natl Acad. Sci. USA* **104**, 20908–20913 (2007).
35. Edgeworth, J. A., Jackson, G. S., Clarke, A. R., Weissmann, C. & Collinge, J. Highly sensitive, quantitative cell-based assay for prions adsorbed to solid surfaces. *Proc. Natl Acad. Sci. USA* **106**, 3479–3483 (2009).
36. Terry, C. et al. Ex vivo mammalian prions are formed of paired double helical prion protein fibrils. *Open Biol.* **6**, 160035 (2016).
37. Terry, C. et al. Structural features distinguishing infectious ex vivo mammalian prions from non-infectious fibrillar assemblies generated in vitro. *Sci. Rep.* **9**, 376 (2019).
38. Hornemann, S. et al. Recombinant full-length murine prion protein, *m*PrP(23–231): purification and spectroscopic characterization. *FEBS Lett.* **413**, 277–281 (1997).
39. Wuthrich, K. & Riek, R. Three-dimensional structures of prion proteins. *Adv. Protein Chem.* **57**, 55–82 (2001).
40. Rodriguez, J. A., Jiang, L. & Eisenberg, D. S. Toward the atomic structure of PrP^{Sc}. *Cold Spring Harb. Perspect. Biol.* **9**, a031336 (2017).
41. Sigurdson, C. J. et al. A molecular switch controls interspecies prion disease transmission in mice. *J. Clin. Invest.* **120**, 2590–2599 (2010).
42. Bett, C. et al. Structure of the β2-α2 loop and interspecies prion transmission. *FASEB J.* **7**, 2868–2876 (2012).
43. Kurt, T. D. et al. Prion transmission prevented by modifying the β2-α2 loop structure of host PrP^{C}. *J. Neurosci.* **34**, 1022–1027 (2014).
44. Kurt, T. D. et al. Human prion protein sequence elements impede cross-species chronic wasting disease transmission. *J. Clin. Invest.* **125**, 1485–1496 (2015).
45. Espinosa, J. C., Marín-Moreno, A., Aguilar-Calvo, P. & Torres, J. M. Met_{166}-Glu_{168} residues in human PrP β2-α2 loop account for evolutionary resistance to prion infection. *Neuropathol. Appl. Neurobiol.* **47**, 506–518 (2021).
46. Asante, E. A. et al. A naturally occurring variant of the human prion protein completely prevents prion disease. *Nature* **522**, 478–481 (2015).
47. Artikis, E., Roy, A., Verli, H., Cordeiro, Y. & Caughey, B. Accommodation of in-register N-linked glycans on prion protein amyloid cores. *ACS Chem. Neurosci.* **11**, 4092–4097 (2020).

Methods

Research governance

Prion purification, cell-based prion bioassay and preparation of cryo-EM grids was conducted at University College London (UCL) in microbiological containment level 3 or level 2 facilities with strict adherence to safety protocols. Work with infectious prion samples at Birkbeck College London was performed using dedicated sample holders and equipment with strict adherence to safety procedures and local risk assessment. Prion samples were transported between laboratories in packaging conforming to UN 3373 Biological Substance, Category B specifications. Frozen brains from mice with clinical prion disease were used to generate purified prion samples. These brain samples were generated by us as part of a previous study[31] in which work with animals was performed in accordance with licenses approved and granted by the UK Home Office (project licenses 70/6454 and 70/7274) and conformed to UCL institutional and ARRIVE guidelines. All experimental protocols were approved by the local research ethics committee of UCL Queen Square Institute of Neurology/National Hospital for Neurology and Neurosurgery.

Preparation of purified ME7 prion rods

Prion-infected brain homogenate was prepared by homogenizing 30 brains from female C57Bl/6 mice terminally infected with the ME7 prion strain in Dulbecco's PBS (D-PBS) lacking Ca^{2+} or Mg^{2+} ions (Gibco) to produce a pool of 130 ml of 10% (w/v) ME7 brain homogenate (designated I21487) using established methods[31]. Purification of ME7 prion rods was performed using the protocol of Wenborn et al.[31] with the exception first implemented in Manka et al.[23] that initial protease digestion was performed using PK in the place of pronase E. Accordingly, 200-µl aliquots of 10% (w/v) ME7 brain homogenate were dispensed into standard 1.5-ml microfuge tubes with screw cap and rubber O-ring. Typically, 12 tubes were processed at a time. Samples were treated with 2 µl of 5 mg ml^{-1} PK prepared in water (to give 50 µg ml^{-1} final protease in the sample) and incubated for 30 minutes at 37 °C with constant agitation, after which digestion was terminated by the addition of 4.1 µl of 100 mM 4-(2-aminoethyl) benzenesulfonyl fluoride hydrochloride (AEBSF) to give 2 mM final concentration in the sample. Then, 206 µl of 4% (w/v) sarkosyl (Calbiochem) in D-PBS and 0.83 µl of benzonase (purity 1; 25,000 U ml^{-1}) were added to give final concentrations in the sample of 2% (w/v) and 50 U ml^{-1}, respectively. After incubation for 10 minutes at 37 °C, 33.5 µl of 4% (w/v) sodium phosphotungstate (NaPTA) prepared in water pH 7.4 was added to give a final concentration of 0.3% (w/v) in the sample. After incubation for 30 minutes at 37 °C, the samples were adjusted (and thoroughly mixed) with 705.3 µl of 60% (w/v) iodixanol and 57.2 µl of 4% (w/v) NaPTA prepared in water pH 7.4, to give final concentrations in the sample of 35% (w/v) and 0.3% (w/v), respectively. After centrifugation for 90 minutes at 16,100*g*, the sample separates into an insoluble pellet fraction (P1), a clarified supernatant (SN1) and a buoyant, partially flocculated, surface layer (SL). One milliliter of SN1 was carefully isolated from each tube, taking extreme care to avoid cross-contamination with either P1 or SL. SN1 was filtered using an Ultrafree HV microcentrifuge filtration unit (0.45-µm pore size Durapore membrane; Millipore, UFC30HV00). This was accomplished by loading 500-µl aliquots of SN1 and centrifugation at 12,000*g* for 30 seconds using one filtration unit per milliliter of SN1. Then, 480-µl aliquots of filtered SN1 were transferred to new 1.5-ml microfuge tubes and thoroughly mixed with an equal volume of 2% (w/v) sarkosyl in D-PBS containing 0.3% (w/v) NaPTA pH 7.4 and incubated for 10 minutes at 37 °C. Samples were then centrifuged for 90 minutes at 16,100*g* to generate an insoluble pellet fraction (P2) and a clarified supernatant (SN2). SN2 was carefully removed and discarded, after which each P2 pellet was resuspended in 10 µl of 5 mM sodium phosphate buffer pH 7.4 containing 0.3% (w/v) NaPTA and 0.1% (w/v) sarkosyl. To avoid unnecessary aggregation of the purified rods arising from repeated rounds of centrifugation, the final two wash steps detailed in Wenborn et al.[31] were replaced with a single wash. Resuspended P2 pellets were pooled and mixed with 1.0 ml of 5 mM sodium phosphate buffer pH 7.4 containing 0.3% (w/v) NaPTA and 0.1% (w/v) sarkosyl, and samples were centrifuged at 16,100*g* for 30 minutes to generate a clarified supernatant (SN3) and an insoluble pellet fraction (P3). SN3 was carefully removed and discarded, and final P3 samples were typically resuspended to a concentration of 150–200× relative to the starting volume of 10% (w/v) brain homogenate from which they were derived, before loading onto EM grids (see below).

Prion infectivity of brain homogenates or purified samples was measured using the Scrapie Cell End Point Assay[31,33–35] using LD9 cells (an established cell line, which was a gift from Charles Weissmann and originally derived from murine L929 fibroblasts supplied by the American Type Culture Collection[34]). Every experiment included concomitant assay of a serial dilution of RML prions of known prion titer determined from rodent bioassay. Ten percent (w/v) RML brain homogenate I6200 was used as the standard and reported a prion titer of $10^{7.3+0.5}$ (mean + s.d.) intracerebral LD_{50} units per milliliter when endpoint titrated six times in Tg20 mice that overexpress mouse PrP on a *Prnp*$^{o/o}$ background[31]. PrP concentrations in purified samples were measured by ELISA[31].

SDS-PAGE, silver staining and western blotting

Samples were prepared for SDS-PAGE using NuPAGE 4× LDS buffer and 10× Reducing Agent (Thermo Fisher Scientific) according to the manufacturer's instructions, followed by immediate transfer to a 100 °C heating block for 10 minutes. Electrophoresis was performed on NuPAGE 12% Bis-Tris protein gels (Thermo Fisher Scientific), run for 60 minutes at 200 V, before electroblotting to Immobilon P membrane (Millipore) for 16 hours at 15 V. Membranes were blocked in 1× PBS (prepared from 10× concentrate; VWR International) containing 0.05% (v/v) Tween 20 (PBST) and 5% (w/v) non-fat dried skimmed milk powder and then probed with 0.2 µg ml^{-1} of anti-PrP monoclonal antibody ICSM35 (D-Gen Ltd.) in PBST for at least 1 hour. After washing (1 hour with PBST), the membranes were probed with a 1:10,000 dilution of alkaline-phosphatase-conjugated goat anti-mouse IgG secondary antibody (Sigma-Aldrich, A2179) in PBST. After washing (1 hour with PBST and 2 × 5 minutes with 20 mM Tris pH 9.8 containing 1 mM $MgCl_2$), blots were incubated for 5 minutes in chemiluminescent substrate (CDP-Star, Tropix Inc.) and visualized on Biomax MR film (Carestream). SDS-PAGE gels (prepared as above) were silver stained using the Pierce Silver Stain Kit (Thermo Fisher Scientific) according to the manufacturer's instructions. Gels were photographed on a light box using a Nikon Coolpix P6000 digital camera. Typical sample loadings for western blotting or silver staining correspond to purified material derived from 10 µl or 100 µl of 10% (w/v) prion-infected brain homogenate per lane, respectively. The SDS-PAGE and western blot data generated in this study are provided in a Source Data file.

ME7 sample preparation for cryo-EM

ME7 prion rods purified from 2.4 ml of 10% (w/v) ME7-infected brain homogenate were resuspended from the P3 pellet (see above) in 10–20 µl of 5 mM sodium phosphate buffer pH 7.4 containing 0.1% (w/v) sarkosyl, and 4 µl of the suspension was applied directly to a glow-discharged C-flat Holey Carbon CF-2/2-4C Cu 400 mesh cryo-EM grid (Electron Microscopy Sciences) or Quantifoil R2/2 Cu 300 mesh grids in the chamber of the Leica GP2 plunging robot. The chamber was set to 20 °C and 40% humidity. After 10-second incubation, the grids were blotted for 3 seconds (with an additional 2-mm push) and plunge-frozen in liquid ethane maintained at −183 °C.

Cryo-EM data collection

Cryo-micrographs were acquired at Birkbeck College London on a 300-kV Krios G3i microscope (FEI/Thermo Fisher Scientific) with a post-GIF (20-eV slit) K3 detector (Gatan) operated in super-resolution

bin 2× mode at 105,000 nominal magnification. The final (post-binning) magnified pixel size was 0.828 Å. The dose rate was ~19.9 e-/Å^2/s during 2.5-second exposures, resulting in a total dose of ~49.75 e-/Å^2 on the specimen. The exposures were collected automatically at five shots per grid hole, with fast acquisition (up to ~370 images per hour), using the EPU 2 software (FEI/Thermo Fisher Scientific), at defocus ranging from 2.4 µm to 0.9 µm and fractionated into 50 movie frames.

Cryo-EM image processing and 3D reconstruction

All image processing except filament picking was done within the RELION 4.0-beta framework[48]. We used RELION's implementation of the MotionCor2 algorithm to align movie frames. The contrast transfer function (CTF) parameters were estimated with CTFFIND4 (ref. 49). We then trained the deep learning package crYOLO[50] to pick ME7 filaments using 100 example micrographs, as previously reported[23]. We imported the coordinates into RELION and extracted images of prion rod segments with different box sizes (ranging from 1,024 to 384 pixels) to perform reference-free two-dimensional (2D) classifications. Optimal 2D class averages and segments were selected for further processing and used to de novo generate an initial 3D reference with the relion_helix_inimodel2d program[51], using an estimated rise of 4.79 Å and helical twist according to the observed crossover distances of the filaments in the 2D class averages. After 3D classification and 3D auto-refinement, we obtained a 3D reconstruction of the ME7 protofibril at 2.9-Å resolution. Subsequent Bayesian polishing[52] and CTF refinement[53] were performed to further improve the resolution of the reconstruction to 2.6 Å, according to the 0.143 Fourier shell correlation (FSC) cutoff criterion (Supplementary Fig. 2). The final 3D map was sharpened with a generous, soft-edged solvent mask at 10% of the height of the box using the computed B-factor value of −26.75 Å^2. The sharpened map was used for the subsequent atomic model building and refinement. The absolute hand of the helical twist was determined directly from the map through resolved densities of the carbonyl oxygen atoms of the polypeptide backbone[51]. The local resolution calculation was performed by LocRes in RELION 4.0-beta with solvent mask over the entire map.

Atomic model building and refinement

A single subunit repeat was extracted from the cryo-EM map of the ME7 protofibril in UCSF Chimera[54]. A single PrP chain from the previously determined atomic model of the RML fibril structure (Protein Data Bank (PDB) ID: 7QIG)[23] was C-terminally extended by addition of D226–R229 residues and fitted to the extracted ME7 density in Coot[55]. The initially fitted atomic model was then copied and fitted into three consecutive subunits in the ME7 map, and the map was zoned around the atomic coordinates in UCSF Chimera[54]. The three-rung map and model were placed in a new unit cell with P1 space group for subsequent model refinement using default settings in phenix.real_space_refine[56] and REFMAC5 (ref. 57). Model geometry was evaluated using MolProbity[58] (http://molprobity.biochem.duke.edu/) after each round of refinement, and problematic or poorly fitting regions in the model were manually adjusted using Coot[55] and ISOLDE[59] (within ChimeraX[60]). This process was repeated until a satisfactory level of model:map agreement with acceptable model stereochemistry was achieved (Supplementary Table 2).

Structure analyses and presentation

Analyses and visualizations of the cryo-EM density map and the models compared in this study were done using UCSF Chimera[54] and ChimeraX[60].

Determination of N-terminal PK cleavage sites by mass spectrometry

N-terminal PK cleavage sites in PrP subunits of ME7 fibrils were determined by targeted derivatization of α-amino groups and subsequent analysis by mass spectrometry as done previously for RML fibrils[23]. In brief, purified ME7 fibrils were electrophoresed in NuPAGE 12% Bis-Tris mini protein gels (Thermo Fisher Scientific), after which gel sections spanning all three PrP glycoforms were excised. Gel pieces were reduced with 100 µM tris(2-carboxyethyl)phosphine and alkylated with 200 µm of iodoacetamide before N-terminal labeling with 6 mM N-succinimidyloxycarbonylmethyl tris(2,4,6-trimethoxyphenyl)phosphonium bromide (TMPP-Ac-OSu) (Sigma-Aldrich) for 1 hour at 22 °C in 100 mM HEPES buffer pH 8.2. After washing, gel pieces were digested overnight with trypsin at a working concentration of 2.5 µg ml^{-1}. Tryptic digest peptides were recovered from the gel and analyzed by liquid chromatography–mass spectrometry, using an Acquity I-Class UPLC system coupled to a Xevo G2-XS Q-ToF mass spectrometer (Waters). Data were collected in MSe acquisition mode using concurrent low-collision and high-collision energy functions with 5 V and 15–45 V of collision energy, respectively. ProteinLynx Global Server 3.0.3 (Waters) and a species-specific reference proteome (UniProt UP000000589, *Mus musculus*) were used to assign peptide sequences optionally allowing for N-terminal amino-group derivatization by TMPP (+572.1811 Da). For each TMPP-labeled peptide, extracted ion chromatograms were generated, and their relative abundance was determined from their respective peak areas. These data are provided in a Source Data file.

Statistics and reproducibility

Purification of ME7 prions was successfully replicated ~30 times while optimizing sample concentrations for cryo-freezing using a 120-kV Talos microscope (FEI/Thermo Fisher Scientific). Eight cryo-EM grids containing material from four independent prion purifications were used for data collection in the Krios G3i microscope. Representative images of prion rods in ice were selected from a dataset comprising 6,370 multi-frame movies.

Reporting summary

Further information on research design is available in the Nature Portfolio Reporting Summary linked to this article.

Data availability

The ME7 cryo-EM density map was deposited into the Electron Microscopy Data Bank (EMDB) (https://www.ebi.ac.uk/pdbe/emdb) under accession number EMD-15043 (Infectious mouse-adapted ME7 scrapie prion fibril purified from terminally-infected mouse brains). The corresponding atomic coordinates were deposited in the Protein Data Bank (PDB) (https://www.rcsb.org) under PDB ID 8A00. The RML 3D cryo-EM density map was accessed from the EMDB under accession number EMD-13989 (Infectious mouse-adapted RML scrapie prion fibril purified from terminally-infected mouse brains). The corresponding atomic coordinates were accessed from the PDB under PDB ID 7QIG. The atomic coordinates of the hamster 263K prion fibril (infectious mammalian prion fibril: 263K scrapie) were accessed from the PDB under ID 7LNA. UniProt UP000000589, *Mus musculus*, was used as the reference proteome for mass spectrometry. Uncropped and unprocessed SDS-PAGE and western blot data and mass spectrometry data generated in this study are provided in the Source Data files. Source data are provided with this paper.

References

48. Kimanius, D., Dong, L., Sharov, G., Nakane, T. & Scheres, S. H. W. New tools for automated cryo-EM single-particle analysis in RELION-4.0. *Biochem. J.* **478**, 4169–4185 (2021).
49. Rohou, A. & Grigorieff, N. CTFFIND4: fast and accurate defocus estimation from electron micrographs. *J. Struct. Biol.* **192**, 216–221 (2015).
50. Wagner, T. et al. Two particle-picking procedures for filamentous proteins: SPHIRE-crYOLO filament mode and SPHIRE-STRIPER. *Acta Crystallogr. D Struct. Biol.* **76**, 613–620 (2020).

51. Scheres, S. H. W. Amyloid structure determination in RELION-3.1. *Acta Crystallogr. D Struct. Biol.* **76**, 94–101 (2020).
52. Zivanov, J., Nakane, T. & Scheres, S. H. W. A Bayesian approach to beam-induced motion correction in cryo-EM single-particle analysis. *IUCrJ* **6**, 5–17 (2019).
53. Zivanov, J., Nakane, T. & Scheres, S. H. W. Estimation of high-order aberrations and anisotropic magnification from cryo-EM data sets in RELION-3.1. *IUCrJ* **7**, 253–267 (2020).
54. Pettersen, E. F. et al. UCSF Chimera—a visualization system for exploratory research and analysis. *J. Comput. Chem.* **25**, 1605–1612 (2004).
55. Emsley, P., Lohkamp, B., Scott, W. G. & Cowtan, K. Features and development of Coot. *Acta Crystallogr. D Biol. Crystallogr.* **66**, 486–501 (2010).
56. Afonine, P. V. et al. Real-space refinement in PHENIX for cryo-EM and crystallography. *Acta Crystallogr. D Struct. Biol.* **74**, 531–544 (2018).
57. Murshudov, G. N. et al. REFMAC5 for the refinement of macromolecular crystal structures. *Acta Crystallogr. D Biol. Crystallogr.* **67**, 355–367 (2011).
58. Williams, C. J. et al. MolProbity: more and better reference data for improved all-atom structure validation. *Protein Sci.* **27**, 293–315 (2018).
59. Croll, T. I. ISOLDE: a physically realistic environment for model building into low-resolution electron-density maps. *Acta Crystallogr. D Struct. Biol.* **74**, 519–530 (2018).
60. Pettersen, E. F. et al. UCSF ChimeraX: structure visualization for researchers, educators, and developers. *Protein Sci.* **30**, 70–82 (2021).

Acknowledgements

This work was funded by the core award to the MRC Prion Unit at UCL from the UK Medical Research Council (MC_U12316055 and MC_UU_00024/5 to J.D.F.W). Cryo-EM data for this investigation were collected at the Institute of Structural and Molecular Biology Electron Microscopy facility (Birkbeck College, University of London) with financial support from the Wellcome Trust (202679/Z/16/Z, 206166/Z/17/Z and 106249/Z/14/Z to H.R.S). We are very grateful to N. Lukoyanova and S. Chen at Birkbeck College for EM support and to D. Johnson and P. King at UCL for infrastructure support.

Author contributions

J.C., J.D.F.W. and H.R.S. acquired funding and oversaw the study. J.D.F.W. administered the project. S.W.M. and J.D.F.W. supervised the research. S.W.M., A.W., J.B. and J.D.F.W. designed experiments. J.D.F.W. and S.J. generated prion stock homogenates. A.W. and J.B. purified prion rods and performed the mass spectrometry. S.W.M. generated cryo-EM grids. S.W.M. and A.W. processed and analyzed cryo-EM data. S.W.M. reconstructed and refined the cryo-EM map and built and refined the atomic model. S.W.M., A.W., H.R.S., J.D.F.W. and J.C. interpreted results. S.W.M. and J.D.F.W. wrote the manuscript, with contributions from A.W., H.R.S. and J.C.

Competing interests

J.C. is a Director and J.C. and J.D.F.W. are shareholders of D-Gen Ltd., an academic spin-out company working in the field of prion disease diagnosis, decontamination and therapeutics. D-Gen supplied the ICSM35 and ICSM18 antibodies used for western blot and ELISA performed in this study. The other authors declare no potential conflicts of interest.

Additional information

Extended data is available for this paper at https://doi.org/10.1038/s41589-022-01229-7.

Supplementary information The online version contains supplementary material available at https://doi.org/10.1038/s41589-022-01229-7.

Correspondence and requests for materials should be addressed to Helen R. Saibil, John Collinge or Jonathan D. F. Wadsworth.

Peer review information *Nature Chemical Biology* thanks Witold Surewicz and the other, anonymous, reviewer(s) for their contribution to the peer review of this work.

https://doi.org/10.1038/s41589-022-01229-7

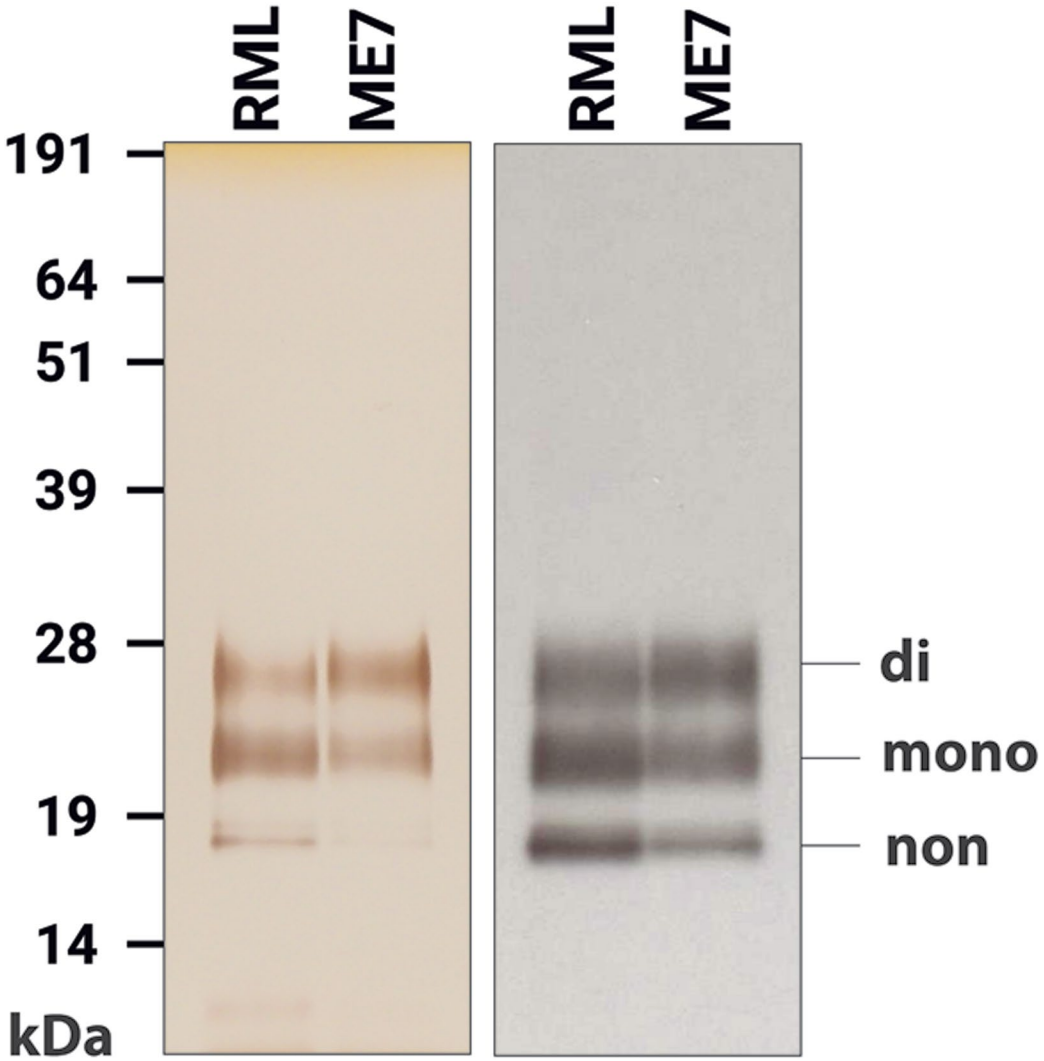

Extended Data Fig. 1 | Silver-stained SDS-PAGE (left) and western blot (right) of purified ME7 and RML rods. Labelling shows the migration positions of di-, mono- and non-glycosylated PrP. The samples were prepared as described in Methods. Uncropped and unprocessed SDS-PAGE and western blot data are provided in a Source Data file. Findings are representative of ~30 purifications.

https://doi.org/10.1038/s41589-022-01229-7

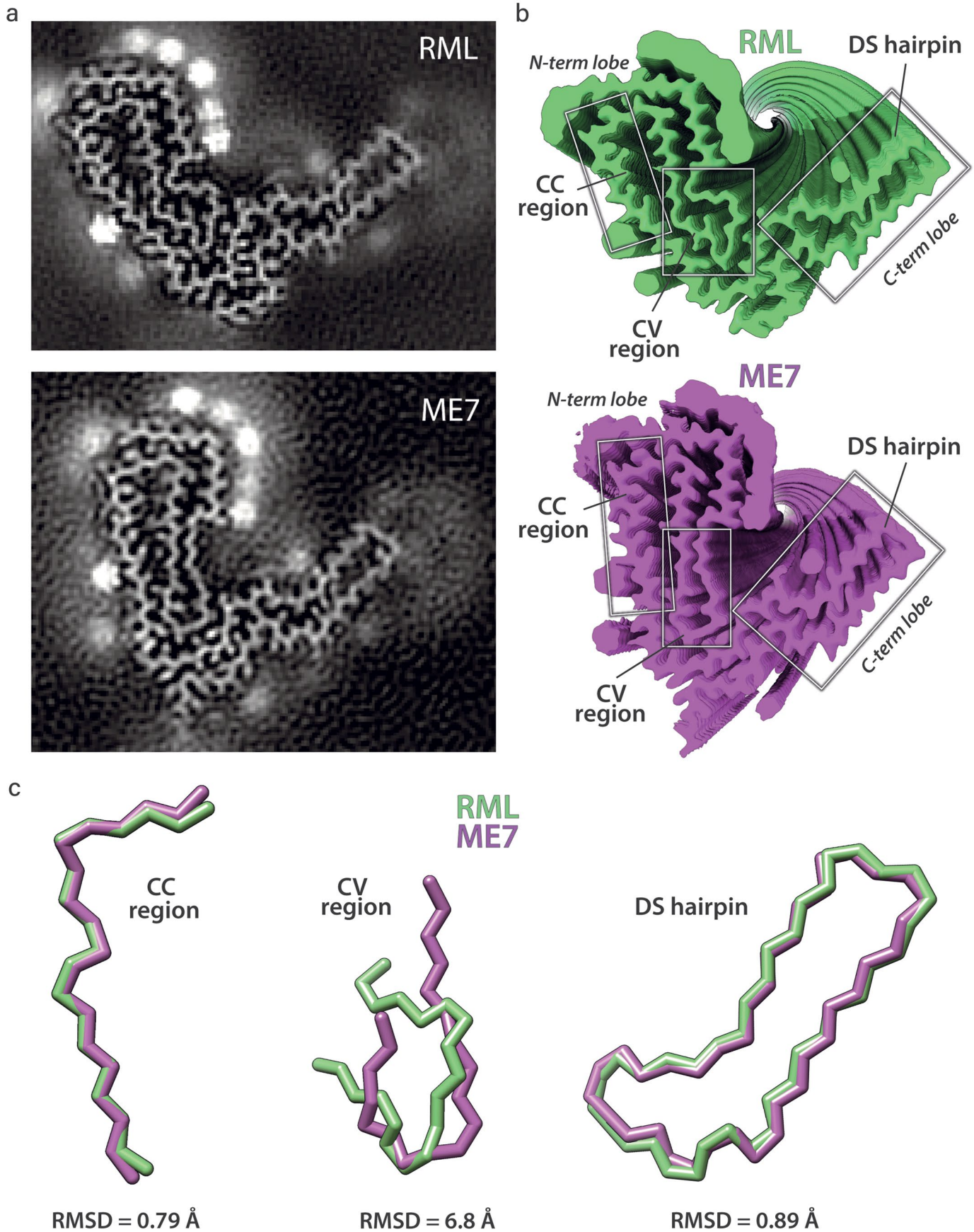

Extended Data Fig. 2 | Comparisons between cryo-EM maps and atomic models of mouse prion fibrils. a Density cross-sections (pixel size: RML, 1.067 Å; ME7, 0.828 Å) showing the protein core and the non-protein extra densities in the final cryo-EM map. **b** Top views of rendered reconstructions with indicated common folding sub-domains. **c** backbone alignments of the common folding sub-domains and the root mean square deviations (RMSD) between all of their respective atom pairs, as calculated using UCSF Chimera[60]. CC, conformationally conserved; CV, conformationally variable; DS, disulphide-stapled.

https://doi.org/10.1038/s41589-022-01229-7

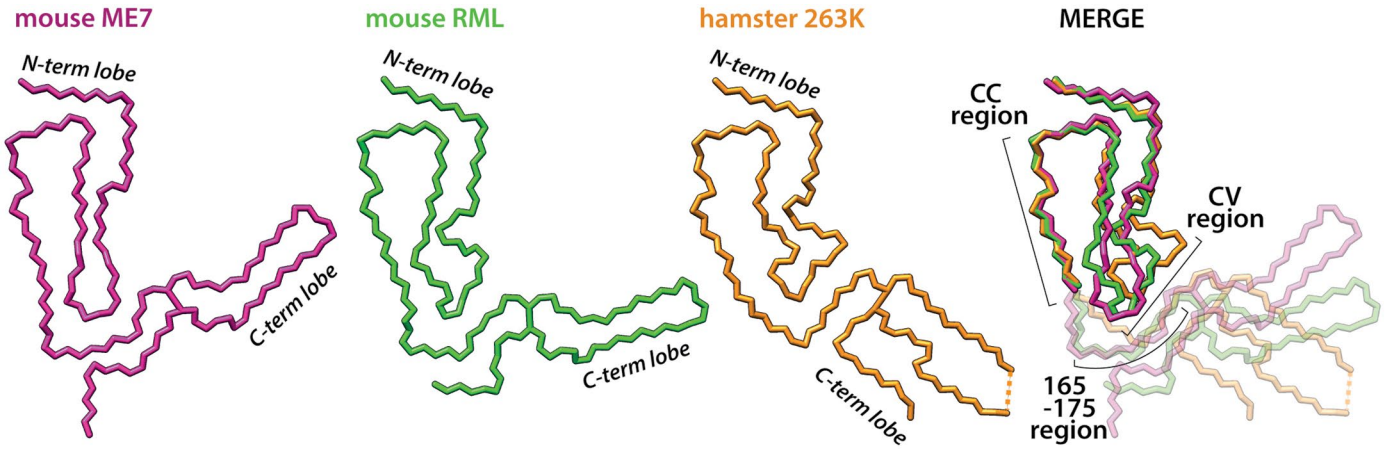

Extended Data Fig. 3 | Comparison of rodent prion structures. Backbones of the three structures are aligned on the conformationally conserved (CC) region in the N-terminal lobe (MERGE, dimmed beyond the CC region). The C-terminal lobe of mouse prion strains has divergent orientations in line with differences in the N-terminal lobe's conformationally variable (CV) region that interfaces with the C-terminal lobe. The C-terminal lobe of the hamster strain diverges further from the mouse strains due to additional differences in its primary structure (PrP sequence). The 165-176 region, which corresponds to the β2-α2 loop in PrP^{C}, is part of the inter-lobe interface in all three rodent prion fibril structures.

nature portfolio

Corresponding author(s): Helen Saibil, John Collinge and Jonathan Wadsworth

Last updated by author(s): Nov 7, 2022

Reporting Summary

Nature Portfolio wishes to improve the reproducibility of the work that we publish. This form provides structure for consistency and transparency in reporting. For further information on Nature Portfolio policies, see our Editorial Policies and the Editorial Policy Checklist.

Statistics

For all statistical analyses, confirm that the following items are present in the figure legend, table legend, main text, or Methods section.

n/a	Confirmed	
☐	☒	The exact sample size (*n*) for each experimental group/condition, given as a discrete number and unit of measurement
☐	☒	A statement on whether measurements were taken from distinct samples or whether the same sample was measured repeatedly
☒	☐	The statistical test(s) used AND whether they are one- or two-sided *Only common tests should be described solely by name; describe more complex techniques in the Methods section.*
☒	☐	A description of all covariates tested
☒	☐	A description of any assumptions or corrections, such as tests of normality and adjustment for multiple comparisons
☐	☒	A full description of the statistical parameters including central tendency (e.g. means) or other basic estimates (e.g. regression coefficient) AND variation (e.g. standard deviation) or associated estimates of uncertainty (e.g. confidence intervals)
☒	☐	For null hypothesis testing, the test statistic (e.g. *F*, *t*, *r*) with confidence intervals, effect sizes, degrees of freedom and *P* value noted *Give P values as exact values whenever suitable.*
☒	☐	For Bayesian analysis, information on the choice of priors and Markov chain Monte Carlo settings
☒	☐	For hierarchical and complex designs, identification of the appropriate level for tests and full reporting of outcomes
☒	☐	Estimates of effect sizes (e.g. Cohen's *d*, Pearson's *r*), indicating how they were calculated

Our web collection on statistics for biologists contains articles on many of the points above.

Software and code

Policy information about availability of computer code

Data collection	EPU 2 (version 2; Thermo Fisher)
Data analysis	Relion 4.0-beta (MRC-LMB, Cambridge), crYOLO 1.8.2. (Wagner et al., 2019), CTFFIND4.1 (Rohou and Grigorieff, 2015), Coot 0.9.6 (Emsley et al., 2010), PHENIX 1.19.2 (Afonine et al., 2018), REFMAC5 5.5 (Murshudov et al., 2011), ISOLDE 1.2 (Croll, 2018), MolProbity 4.5.1 (Williams et al., 2018), UCSF Chimera 1.15 (Pettersen et al., 2004), UCSF ChimeraX 1.1.1 (Pettersen et al., 2021), ProteinLynx Global Server 3.0.3 (Waters)

For manuscripts utilizing custom algorithms or software that are central to the research but not yet described in published literature, software must be made available to editors and reviewers. We strongly encourage code deposition in a community repository (e.g. GitHub). See the Nature Portfolio guidelines for submitting code & software for further information.

Data

Policy information about availability of data

All manuscripts must include a data availability statement. This statement should provide the following information, where applicable:

- Accession codes, unique identifiers, or web links for publicly available datasets
- A description of any restrictions on data availability
- For clinical datasets or third party data, please ensure that the statement adheres to our policy

The ME7 cryo-EM density map was deposited into the Electron Microscopy Data Bank (https://www.ebi.ac.uk/pdbe/emdb) under accession code EMD-15043 (Infectious mouse-adapted ME7 scrapie prion fibril purified from terminally-infected mouse brains). The corresponding atomic coordinates were deposited in the

Protein Data Bank (https://www.rcsb.org) under PDB code 8A00. The RML 3D cryo-EM density map was accessed from the EMDB (https://www.ebi.ac.uk/pdbe/emdb) under accession no. EMD-13989 [https://www.ebi.ac.uk/pdbe/entry/emdb/EMD-13989] (Infectious mouse-adapted RML scrapie prion fibril purified from terminally-infected mouse brains). The corresponding atomic coordinates were accessed from the PDB (https://www.rcsb.org) under PDB code 7QIG [https://doi.org/10.2210/pdb7QIG/pdb]. The atomic coordinates of the hamster 263K prion fibril (infectious mammalian prion fibril: 263K scrapie) was accessed from PDB under code 7LNA [https://doi.org/10.2210/pdb7lna/pdb]. Uniprot UP000000589, mus musculus was used as the reference proteome for mass spectrometry [https://www.uniprot.org/proteomes/UP000000589]. Uncropped and unprocessed SDS-PAGE and western blot data and mass spectrometry data generated in this study are provided in Source Data files.

Human research participants

Policy information about studies involving human research participants and Sex and Gender in Research.

Reporting on sex and gender	n/a
Population characteristics	n/a
Recruitment	n/a
Ethics oversight	n/a

Note that full information on the approval of the study protocol must also be provided in the manuscript.

Field-specific reporting

Please select the one below that is the best fit for your research. If you are not sure, read the appropriate sections before making your selection.

☒ Life sciences ☐ Behavioural & social sciences ☐ Ecological, evolutionary & environmental sciences

For a reference copy of the document with all sections, see nature.com/documents/nr-reporting-summary-flat.pdf

Life sciences study design

All studies must disclose on these points even when the disclosure is negative.

Sample size	Sample size (the number of particle images or segments) was not predetermined. We aimed to collect ~6,000 multi-frame movies as this was expected to provide sufficient particles for high resolution 3D reconstruction. This was achieved. Satisfactory sample size is reflected in the final near-atomic and isotropic resolution of the 3D reconstruction, sufficient for building and refining an atomic model.
Data exclusions	In single-particle cryo-EM data processing so called 'bad particles' are excluded due to their obvious poor quality, which precludes their alignment with the consensus data. The sparse regions of micrographs where sample image quality is poor (for example, due to grid surface contamination giving rise to local noise in particle image or due to sample heterogeneity) would ideally be not selected for processing, but this cannot be avoided, especially when using automated particle picking, as in this study. Image processing algorithms reveal such poor particles as not classifiable under objective computational criteria into any biologically relevant class, which objectifies exclusion.
Replication	30 infected mouse brains were combined to produce one brain homogenate. The final cryo-EM dataset combined images from 4 independent rounds of purification of ME7 fibrils from this brain homogenate. The purification method was first reported in 2015 (Wenborn et al Sci Rep 2015) and with minor modifications in 2022 (Manka et al 2022). The method is robust and we have had no replication failures after >100 repetitions. The method has also been independently used and replicated in other laboratories. In this study the method had no replication failures during ~30 purifications of ME7 prions.
Randomization	Since only one homogeneous state was targeted randomization is not relevant to this study.
Blinding	Classifications of particle images were performed computationally and therefore objectively. Blinding was not relevant for prion purification and sample characterization as there was only one type of prion sample.

Reporting for specific materials, systems and methods

We require information from authors about some types of materials, experimental systems and methods used in many studies. Here, indicate whether each material, system or method listed is relevant to your study. If you are not sure if a list item applies to your research, read the appropriate section before selecting a response.

Materials & experimental systems

n/a	Involved in the study
☐	☒ Antibodies
☐	☒ Eukaryotic cell lines
☒	☐ Palaeontology and archaeology
☐	☒ Animals and other organisms
☒	☐ Clinical data
☒	☐ Dual use research of concern

Methods

n/a	Involved in the study
☒	☐ ChIP-seq
☒	☐ Flow cytometry
☒	☐ MRI-based neuroimaging

Antibodies

Antibodies used

ICSM 35 mouse anti-PrP monoclonal antibody was used for western blotting (at 0.2µg/ml concentration) in conjunction with alkaline-phosphatase-conjugated goat anti-mouse IgG secondary antibody (Sigma-Aldrich, Cat No A2179 at 1:10,000 dilution). ICSM 35 and ICSM 18 mouse anti-PrP monoclonal antibodies were used for determination of PrP concentration by ELISA using previously published methods (Wenborn et al 2015). Concentrations of ICSM 35 and ICSM 18 used for ELISA are detailed in (Wenborn et al 2015). ICSM 35 and ICSM 18 antibodies were supplied by D-Gen Ltd, London and details of their production and characterisation are provided in Khalili-Shirazi et al. Biochim Biophys Acta. 2007;1774:1438-50. Numerous other anti-PrP antibodies from commercial or academic sources could be used for these purposes and there is no reliance on the particular properties of ICSM 35 and ICSM 18.

Validation

Validation is provided in Wenborn et al 2015 and references cited therein.

Eukaryotic cell lines

Policy information about cell lines and Sex and Gender in Research

Cell line source(s)

LD9 cells, an established cell line derived from murine L929 fibroblasts (Mahal et al 2007), were provided as a gift from Professor Charles Weissmann. LD9 cells were used to measure prion infectivity in cell culture using previously published methods (Mahal et al 2007; Wenborn et al 2015).

Authentication

LD9 cells (gifted to us by Professor Charles Weissmann) originated from murine L929 fibroblasts that were supplied and authenticated by the American Type Culture Collection (ATCC) (Mahal et al 2007). The original L929 fibroblasts supplied by ATCC were not used in this study. LD9 cells used by us were not authenticated.

Mycoplasma contamination

LD9 cells have been tested negative for mycoplasma contamination.

Commonly misidentified lines
(See ICLAC register)

None

Animals and other research organisms

Policy information about studies involving animals; ARRIVE guidelines recommended for reporting animal research, and Sex and Gender in Research

Laboratory animals

30 female C57Bl/6 mice, ~210 days old, terminally-infected with ME7 prions.

Wild animals

n/a

Reporting on sex

Only female mice were used

Field-collected samples

n/a

Ethics oversight

Frozen brains from mice with clinical prion disease were used to generate purified prion samples. These brain samples were generated by us as part of a previous study (Wenborn et al 2015) in which work with animals was performed in accordance with licences approved and granted by the UK Home Office (Project Licences 70/6454 and 70/7274) and conformed to University College London institutional and ARRIVE guidelines. All experimental protocols were approved by the Local Research Ethics Committee of UCL Queen Square Institute of Neurology/National Hospital for Neurology and Neurosurgery.

Note that full information on the approval of the study protocol must also be provided in the manuscript.